PNAS RESEARCH ARTICLE | BIOCHEMISTRY OPEN ACCESS

Cryo-EM structure of the four-subunit *Rhodobacter sphaeroides* cytochrome bc_1 complex in styrene maleic acid nanodiscs

David J. K. Swainsbury[a,b,1], Frederick R. Hawkings[b,c], Elizabeth C. Martin[b], Sabina Musial[b,2], Jack H. Salisbury[b], Philip J. Jackson[b], David A. Farmer[c], Matthew P. Johnson[b], C. Alistair Siebert[c], Andrew Hitchcock[b], and C. Neil Hunter[b]

Edited by Yifan Cheng, University of California San Francisco, San Francisco, CA; received November 1, 2022; accepted February 1, 2023

Cytochrome bc_1 complexes are ubiquinol:cytochrome *c* oxidoreductases, and as such, they are centrally important components of respiratory and photosynthetic electron transfer chains in many species of bacteria and in mitochondria. The minimal complex has three catalytic components, which are cytochrome *b*, cytochrome c_1, and the Rieske iron–sulfur subunit, but the function of mitochondrial cytochrome bc_1 complexes is modified by up to eight supernumerary subunits. The cytochrome bc_1 complex from the purple phototrophic bacterium *Rhodobacter sphaeroides* has a single supernumerary subunit called subunit IV, which is absent from current structures of the complex. In this work we use the styrene–maleic acid copolymer to purify the *R. sphaeroides* cytochrome bc_1 complex in native lipid nanodiscs, which retains the labile subunit IV, annular lipids, and natively bound quinones. The catalytic activity of the four-subunit cytochrome bc_1 complex is threefold higher than that of the complex lacking subunit IV. To understand the role of subunit IV, we determined the structure of the four-subunit complex at 2.9 Å using single particle cryogenic electron microscopy. The structure shows the position of the transmembrane domain of subunit IV, which lies across the transmembrane helices of the Rieske and cytochrome c_1 subunits. We observe a quinone at the Q_o quinone-binding site and show that occupancy of this site is linked to conformational changes in the Rieske head domain during catalysis. Twelve lipids were structurally resolved, making contacts with the Rieske and cytochrome *b* subunits, with some spanning both of the two monomers that make up the dimeric complex.

cytochrome bc_1 | quinone | *Rhodobacter sphaeroides* | evolution | photosynthesis

Cytochrome (cyt) bc_1 complexes are quinol:cytochrome *c* oxidoreductases (E.C. 1.10.2.2) and are central components of respiratory and photosynthetic electron transport chains in bacteria and mitochondria. These multisubunit complexes translocate protons across bioenergetic membranes, generating a proton-motive force (pmf) that can be used to directly power cellular functions (e.g., flagella rotation and substrate transport) or stored in a chemical form as adenosine triphosphate (ATP). Similar to the related cytochrome b_6f complex (cyt b_6f) found in chloroplasts and cyanobacteria, cyt bc_1 complexes operate via a modified Q-cycle, in which oxidation of two quinols at the Q_o site (also known as Q_P) leads to the release of four protons on the positive side of the membrane, the reduction of soluble electron carriers in the lumen/intermembrane space, and the regeneration of a quinol at the Q_i site (also known as Q_n) coupled to the uptake of two protons from the cytoplasm/matrix (1, 2). This bifurcated electron transfer mechanism increases the number of protons translocated per quinol oxidized and explains the high coupling efficiency of cyt bc_1 and cyt b_6f complexes. Quinol oxidation by these complexes is the rate-limiting step in photosynthetic electron transport, further underlying the central importance of cyt bc_1 and cyt b_6f in electron transfer chains (3–11).

The simplest cyt bc_1 complexes, such as the bacterial complexes from *Rhodobacter capsulatus* or *Paracoccus denitrificans,* comprise three subunits: cyt *b*, which binds two *b*-type hemes (b_L and b_H) one quinol and one quinone; cyt c_1 that binds one *c*-type heme; and the Rieske subunit that binds a two-iron two-sulfur cluster (FeS). The two heme-binding domains are static during the Q-cycle, whereas the membrane-extrinsic head of the Rieske subunit is mobile and undergoes a conformational change during turnover (12, 13). These three catalytic subunits associate to form a dimer with C2 symmetry, and are common to all Rieske/cyt *b* complexes, but the mitochondrial cyt bc_1 complexes (known as complex III) have a varying number of supernumerary subunits, of which there are seven in yeast and plants and eight in mammals (14). In thermophilic bacteria such as *Aquifex aeolicus,* the cyt c_1 subunit has an additional N-terminal transmembrane helix (TMH) that provides a fused supernumerary component of the complex (15). It is unclear why supernumerary components were recruited during evolution, given that three subunits are sufficient for function.

Significance

Cytochrome bc_1 complexes are found in mitochondria and many species of bacteria and are related to the cytochrome b_6f complexes of plants, algae, and cyanobacteria. The simplest cytochrome bc_1 complexes are comprised of three core proteins, but many have acquired supernumerary subunits during evolution. The cytochrome bc_1 complex of *Rhodobacter sphaeroides* has a unique supernumerary subunit, named subunit IV, which enhances its activity. We have determined the structure of the four-subunit cytochrome bc_1 complex from this model phototroph, which provides insight into how and why cytochrome bc_1 complexes evolved supernumerary subunits. Our structure also reveals the position of bound lipids and rationale for how the binding of quinones to the catalytic sites may coordinate the conformational changes that underpin the Q-cycle.

Author contributions: D.J.K.S., A.H. and C.N.H. designed research; D.J.K.S., F.R.H., E.C.M., S.M., J.H.S., P.J.J., D.A.F., C.A.S., and A.H. performed research; D.J.K.S., F.R.H., S.M., J.H.S., P.J.J., M.P.J., A.H., and C.N.H. analyzed data; D.J.K.S., M.P.J., A.H., and C.N.H. supervision; D.J.K.S., M.P.J., A.H., and C.N.H secured funding; and D.J.K.S., A.H., and C.N.H. wrote the paper.

The authors declare no competing interest.

This article is a PNAS Direct Submission.

[1]To whom correspondence may be addressed. Email: d.swainsbury@uea.ac.uk.

[2]Present address: Department of Biology, University of York, York YO10 5DD, United Kingdom.

This article contains supporting information online at https://www.pnas.org/lookup/suppl/doi:10.1073/pnas.2217922120/-/DCSupplemental.

Published March 13, 2023.

Rhodobacter (R.) sphaeroides belongs to the α-proteobacteria, the class of bacteria thought to be the endosymbiotic progenitors of the mitochondria (16). Illuminating photosynthetic reaction centers (RCs) in native chromatophore membranes from this phototrophic bacterium elicits turnover of cyt bc_1 complexes, providing a level of control that was instrumental for understanding the mechanism of cyt bc_1 and for developing and refining the Q-cycle model; examples include refs. 1 and 17–23, and also a more recent review, ref. 24. Early preparations of this cyt bc_1 complex revealed a supernumerary subunit, which was named subunit IV (SIV) (14, 25–28). The gene that encodes SIV was later found outside of the main *fbcFBC* operon that encodes the catalytic subunits and was named *fbc*Q (29). *fbcQ* encodes a 14.4-kDa, 124-amino acid protein that shares no homology to supernumerary subunits of cyt bc_1 complexes from other species or the similarly named subunit IV (PetD) of the cyt b_6f complex. Through biochemical characterization and deletion of *fbcQ*, SIV was shown to be required for photosynthetic growth. However, since SIV is not required in aerobically grown cells, it appears to be unnecessary for the operation of cyt bc_1 complexes during respiratory electron transfer (30). SIV is predicted to consist of an ~10-kDa soluble domain on the cytoplasmic face of the complex and a C-terminal TMH that is suspected to bind quinone (29, 31–33). The absence of SIV results in lowered activity and increased superoxide production, and the complex becomes less stable following detergent treatment, suggesting that SIV is required to produce a stable and fully active complex during photosynthetic growth (30, 34). Several studies showed that the SIV TMH provides the majority of its function and that specific residues in the helix are essential (35–37). Despite this wealth of biochemical data, the structure and function of SIV remain elusive due to its dissociation during purification, and it is therefore absent from existing crystal structures of the *R. sphaeroides* cyt bc_1 complex (38, 39).

In this study, we applied our recently published approach utilizing styrene maleic acid (SMA) copolymer in place of detergents to achieve solubilization of cyt bc_1 from the chromatophore membranes of photosynthetically grown *R. sphaeroides* (40); SMA extracts membrane protein complexes directly from the native membrane, enclosing them in nanodiscs (41–43). This strategy shows great promise for high-resolution structural determination of membrane proteins (44, 45), and in the case of cyt bc_1 and cyt b_6f complexes it preserves the local membrane environment (40). Following successful purification of active complex, we used cryogenic electron microscopy (cryo-EM) to determine the structure of the four-subunit *R. sphaeroides* cyt bc_1 at 2.9 Å resolution, revealing the position of the TMH of SIV and providing insights into its function. We also resolve a natively bound quinone at the Q_o site and alternative conformations of the Rieske subunits, providing information on structural changes during the Q-cycle. Accompanying biochemical comparisons with the complex lacking SIV suggest a role for this component in stabilizing and enhancing uniquinol:cytochrome *c* oxidoreductase activity.

Results

Purification of Cyt bc_1 in Native Nanodiscs. The cyt bc_1 complex sits in a lipid-rich environment within photosynthetic membranes (4, 40), adjacent to RC-light-harvesting complex 1 (RC-LH1) core complexes (46). We previously showed that SMA preferentially extracts the cyt bc_1 complex from its lipid-rich surroundings within chromatophore membranes, whereas the protein-rich domains containing RC-LH1 and light-harvesting complex 2 (LH2) complexes resist the action of SMA (40). Despite low yields of His_{10}-tagged cyt bc_1 purified by nickel affinity chromatography, we demonstrated that the cyt bc_1 dimer copurified with ~56 annular phospholipids, one ubiquinone and SIV, providing a promising strategy for structural and biochemical characterization of the cyt bc_1 complex in a near-native lipid environment (40), which is imperative given that early work on the *R. sphaeroides* cyt bc_1 complex revealed its sensitivity to removal of lipids (25).

To increase the yields of cyt bc_1 in our preparations, we made several alterations to our previous purification protocol. First, we truncated the C terminus of the zinc transporter ZnuC, which was identified as a major contaminant in our previous work (40), by inserting a premature stop codon into the gene. This protein contains eight His residues within its C-terminal 15 amino acids, which we suspect act as a natural His-tag. Second, we commonly observe that SMA weakens the association of the His-tag with the Ni-NTA resin, so after binding, we washed the nickel column with a lower imidazole concentration to prevent undesired elution of cyt bc_1. Finally, we applied the complexes eluted from the Ni-NTA column to a continuous sucrose density gradient and performed an ultracentrifugation step to separate the cyt bc_1 complexes from contaminating RC-LH1 and LH2, damaged cyt bc_1, and other minor contaminants prior to further purification and buffer exchange by size-exclusion chromatography.

Analysis by sodium dodecyl sulfate–polyacrylamide gel electrophoresis (SDS–PAGE) shows that the cyt bc_1-nanodisc complexes were highly pure, with four major bands corresponding to the three catalytic subunits and SIV (Fig. 1*A*). The presence of all four polypeptides was confirmed by mass spectrometry, with minor contamination, mainly by various other membrane proteins (*SI Appendix*, Table S1). Further analysis of the peptides revealed that SIV is complete, or subject to only limited N-terminal processing (*SI Appendix*, Fig. S1). Clear-native (CN)-PAGE (Fig. 1*B*) showed that the complex was mostly dimeric, with some higher order aggregates and a negligible amount of monomeric complex. UV/Vis/NIR spectra of oxidized and reduced cyt bc_1 gave a *b*- to *c*-type heme ratio of 1.7:1, in good agreement with the expected 2:1 ratio (Fig. 1 *C* and *D*).

Comparison of Cyt bc_1 Activity in the Presence and Absence of SIV. To ensure the complex was active, we performed cyt c_2 reduction assays, which demonstrated the complex was functional in the presence of 250 μM decylubiquinol and 50 μM cyt c_2 (Fig. 1*E*, red). To compare the activity of the four-subunit complex with one without SIV, we produced a strain where the *fbcQ* gene was deleted (hereafter ΔSIV), purified the three-subunit complex (*SI Appendix*, Fig. S2), and performed analogous cyt c_2 reduction assays. The activity of the wild-type (WT) complex was 11 ± 2 μmol cyt c_2 reduced/μmol cyt bc_1/s. In the absence of SIV the activity decreased 63% to 4.0 ± 0.2 μmol cyt c_2 reduced/μmol cyt bc_1/s (Fig. 1*E*, blue), similar to the loss observed in detergent preparations (30). We note that the three-subunit complex has a weaker band corresponding to the Rieske subunit on SDS–PAGE gels, which may reflect damage during preparation or misassembly under photosynthetic growth conditions (*SI Appendix*, Fig. S2).

Overall Architecture of the Four-Subunit Complex. Using the purified and active four-subunit complexes, we prepared cryo-EM grids and collected 15,867 movies from which 4,060,135 particles were picked and subjected to multiple rounds of two-dimensional (2D) and three-dimensional (3D) classification. A single high-quality 3D class with 282,636 particles was refined to yield a C1 map with a global resolution of 2.9 Å. Refinement with imposed C2 symmetry gave no significant improvement in resolution, so we modeled the complex using the C1 map to reveal any asymmetrical features. Final validation statistics are displayed in *SI Appendix*, Table S2.

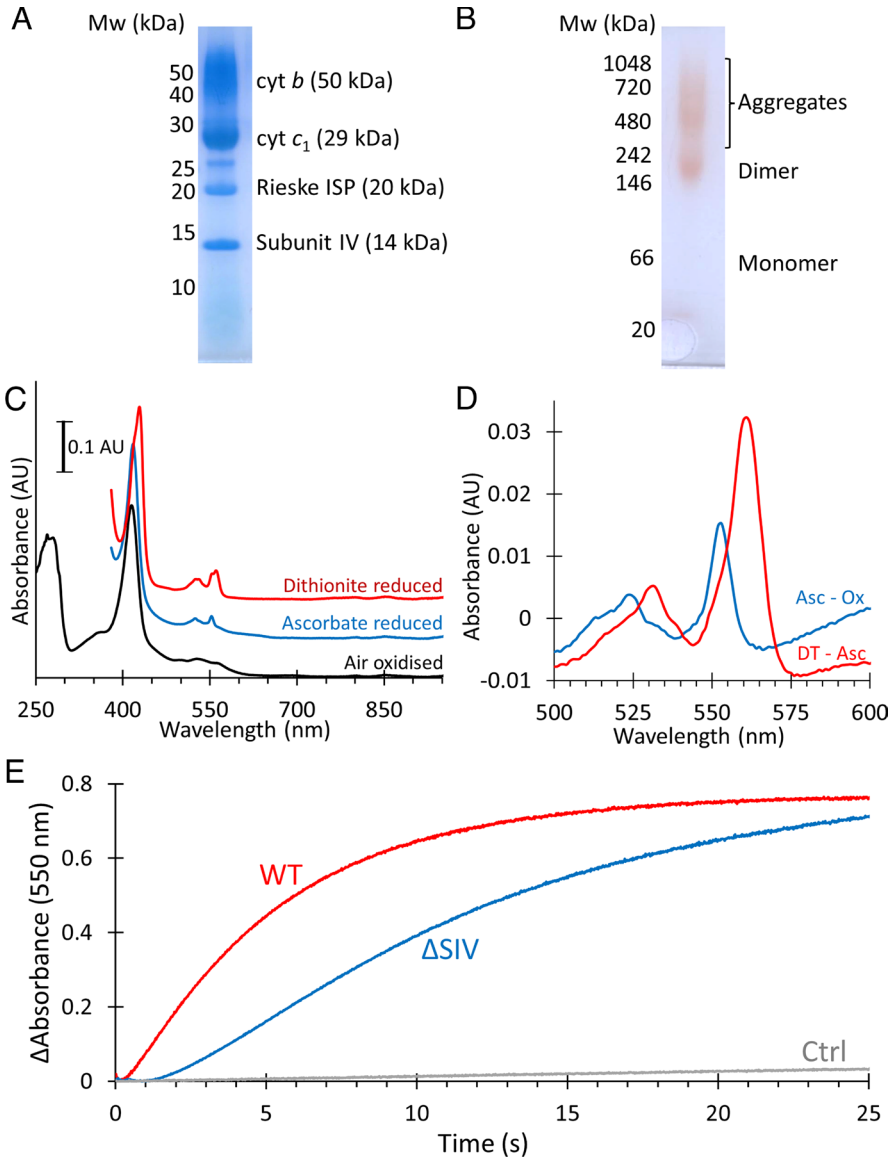

Fig. 1. Purification and characterization of cyt bc_1. (*A*) Coomassie-stained SDS–PAGE of purified cyt bc_1 complexes. Each band is labeled with its identity and predicted mass. (*B*) CN-PAGE of purified cyt bc_1 complexes with the oligomeric state indicated next to the bands. (*C*) UV/Vis/NIR spectra of cyt bc_1 complexes as prepared (Air oxidized) and following the addition of sodium D-ascorbate to reduce *c* hemes, and sodium dithionite to reduce all hemes. (*D*) Ascorbate reduced minus ferricyanide oxidized (Asc – Ox), and dithionite reduced minus ascorbate reduced (DT – Asc) spectra used for determination of *c* and *b* heme concentrations, respectively. (*E*) Activity of purified WT (red) and ΔSIV (blue) complexes, monitored by following the absorption of cyt c_2 at 550 nm. Reactions contained 500 nM cyt bc_1, 50 μM cyt c_2, and 250 μM decylubiquinol (solid lines). The control (Ctrl) reaction performed in the absence of cyt bc_1 shows low spontaneous cyt *c* reduction (gray).

Fig. 2 *A–D* shows the cryo-EM map with colored regions corresponding to the resolved proteins. The dimensions of the dimeric complex in the membrane plane are 100 Å × 93 Å with a height of 96 Å; the complex is surrounded by a 151 Å × 118 Å × 45 Å belt of disordered density corresponding to the SMA-stabilized lipid nanodisc. There are eight TMHs and a b_L and b_H heme for each cyt *b* subunit. The *c* subunits each bind a *c*-type heme within a lumenal soluble domain, which is anchored via a single TMH. The two Rieske iron–sulfur protein (ISP) subunits each consist of one TMH associated with one half of the monomer, and a soluble head domain binding a FeS cluster that interacts with the opposing monomer on the lumenal side of the complex. In the center of the complex is an intermonomer cavity, which is largely empty. Docking an existing crystal structure of the three-subunit *R. sphaeroides* cyt bc_1 complex [PDB ID:2QJP (38)] into the map produced a good agreement between the catalytic subunits of the two structures. The remaining unmodeled regions of the complex revealed a TMH on each side of the complex that, considering fit to density and physical environment, matched to residues 79-107 of SIV (Fig. 2, red). These residues correspond to the predicted transmembrane region with the expected topology, with the N terminus on the cytoplasmic side and the C terminus on the lumenal side (29, 31–33). We also observed 12 ordered lipid molecules, tentatively assigned as 1,2-dioleoyl-*sn*-glycero-3-phosphoethanolamine (PEE), and a ubiquinone-10 molecule bound in the Q_o site of one of the cyt *b* subunits (Fig. 2, gray and pink).

The local resolution of the map was variable with a range of ~2.7 to 4.1 Å. The highest resolution region was for the membrane-embedded cyt *b* subunits, while the soluble head domains of the Rieske subunits and the cytoplasmic region of SIV were at the lowest resolution (*SI Appendix*, Fig. S3), suggesting that these domains may be flexible. It should be noted that we chose not to add inhibitors to our complex in order to retain native quinones and permit the complexes to explore a range of active

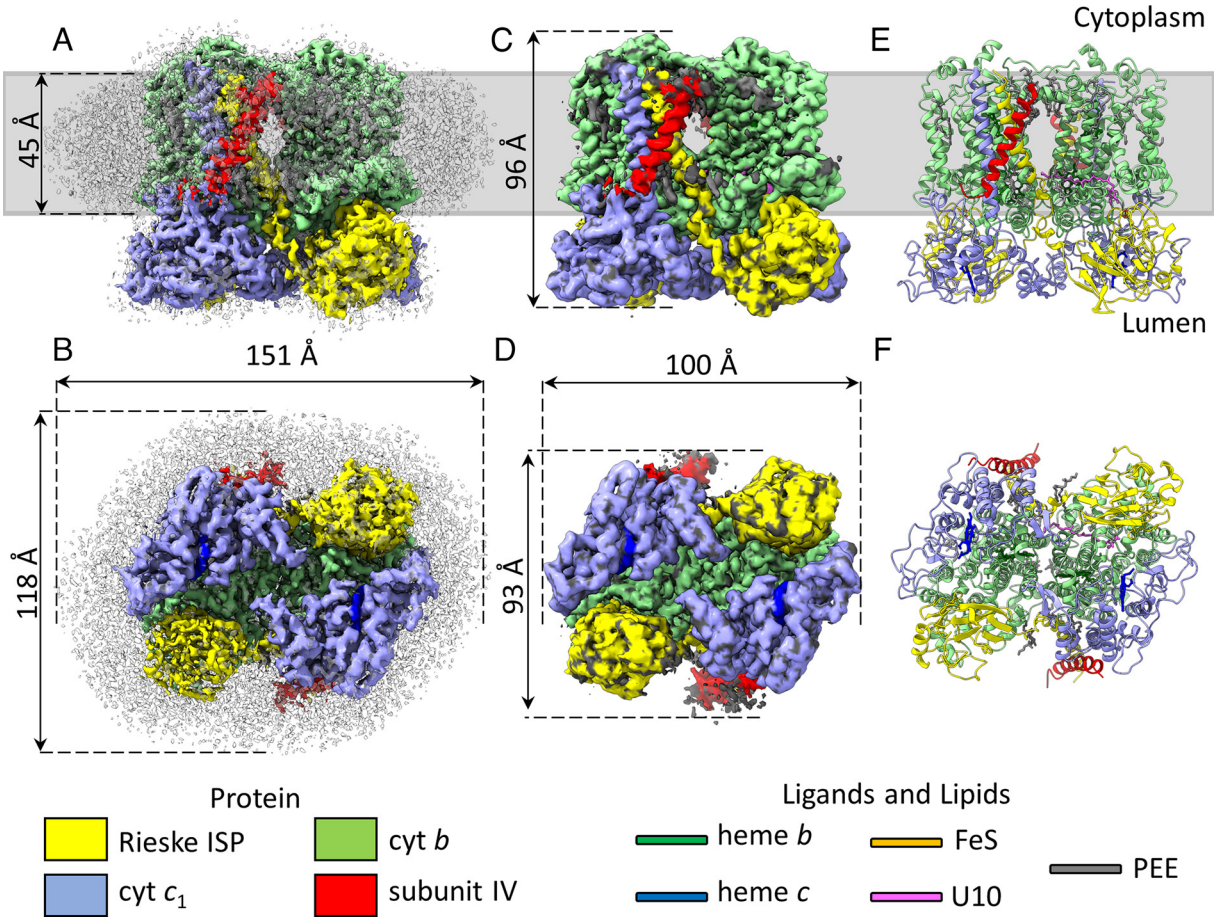

Fig. 2. Color-coded cryo-EM map and refined model for the *R. sphaeroides* four-subunit cyt bc_1 complex. (*A* and *B*) Postprocessed map viewed in the plane of the membrane (*A*) and from the lumenal face (*B*). (*C* and *D*) The map after local sharpening, which removed the disordered density of the nanodisc and improved interpretability for low-resolution portions of the map. (*E* and *F*) The refined model with the protein in cartoon representation, and ligands and lipids in stick representation. The gray bar in panels (*A*, *C*, and *E*) indicates the approximate position of the membrane. U10 = ubiquinone-10 and PEE = 1,2-dioleoyl-sn-glycero-3-phosphoethanolamine.

conformations. To aid interpretation of the map, we applied local sharpening after initial building using LocScale (47), shown in Fig. 2 *C* and *D*, and used this map to further refine the final model shown in Fig. 2 *E* and *F*.

The Structure of Subunit IV. The resolved TMH of SIV is 28 residues in length, corresponding to residues 79 to 107 of the 124-amino acid SIV sequence (Fig. 3*A*). It lies at an angle of ~20 to 25° relative to the membrane plane and interacts extensively with the TMHs of the cyt c_1 and Rieske subunits along most of its inward-facing side (Figs. 2 and 3*B*). Most of the interactions are hydrophobic contacts within the lipid bilayer, with residues 83 to 96 packing against residues 10 to 25 of the Rieske subunit, and residues 95 to 102 packing against residues 253 to 261 of the cyt c_1 subunit. On the lumenal side, there is an additional interaction between Phe107 of SIV and Phe39 within the cyt c_1 head domain (Fig. 3*D*). On the cytoplasmic surface of the complex Arg84 of SIV forms a hydrogen bond with Asp13 of the Rieske subunit (Fig. 3*C*). SIV also makes hydrophobic interactions with the tail of a resolved lipid via the side chains of Phe88 and Ala92 (Fig. 3*C*).

Unexpectedly, no density for the N-terminal 78 residues, corresponding to a molecular mass of ~9.6 kDa, was observed in our refined maps. This region of SIV is predicted to be a small soluble domain on the cytoplasmic side of the membrane. SDS–PAGE suggests SIV has a molecular mass of ~15 kDa, indicating that the N-terminal region is intact in our preparation (Fig. 2*A*), and mass spectrometry shows that peptides corresponding to the unresolved region are present (*SI Appendix*, Fig. S1). We note that the cytoplasmic end of the SIV TMHs has a relatively low local resolution (*SI Appendix*, Fig. S3), and that the backbone extends away from the rest of the complex (Fig. 3 *B* and *C*). Attempts to resolve density for the N-terminal domain of SIV from the cryo-EM data by focused refinement were unsuccessful. We attempted to model the structure of SIV using AlphaFold (48), which predicted a range of conformations for the soluble domain and could not correctly position SIV within the remainder of the complex. Taken together, these data suggest that the SIV N-terminal domain is highly flexible and does not adopt a constant, resolvable conformation with respect to the remainder of the cyt bc_1 complex.

Structurally Resolved Lipids. Following detergent-free extraction of cyt bc_1 from the native membrane with SMA, we aimed to resolve the lipids that copurified with the complex. Twelve lipids were modeled into the map (Fig. 4), all of which were identified by their characteristic fork-shaped density. We were unable to unambiguously model the head groups, so tentatively assigned each as PEE and truncated the lipid tails as necessary to fit the density.

Four lipids were resolved on the lumenal side of the complex in a symmetrical arrangement where two lipids are bound within clefts on either side of the Rieske TMH, below the flexible linker that connects it to the head domain. One of these lipids interacts

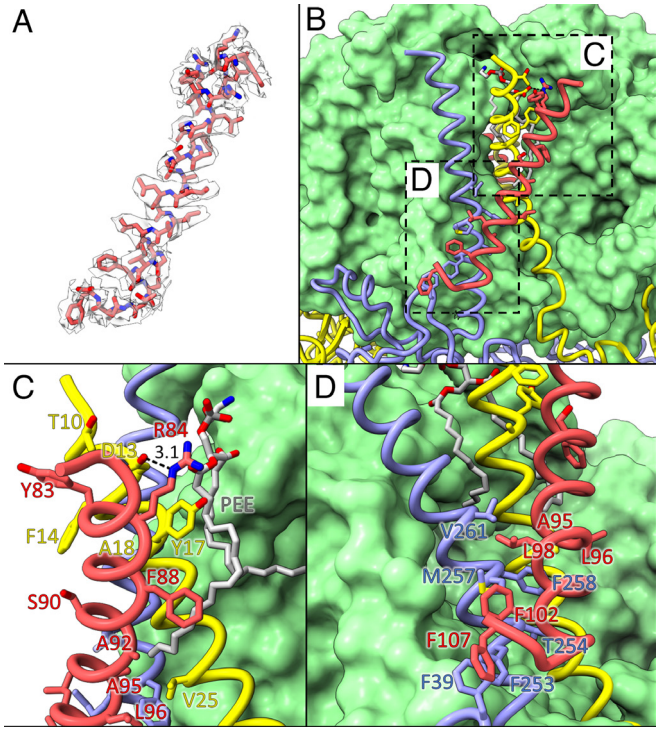

Fig. 3. Structure of the resolved region of SIV and its interactions with the cyt bc_1 complex. (*A*) Model of residues 79 to 107 of subunit IV (sticks) within its density after local sharpening (semi-transparent surface). (*B*) Expanded view of subunit IV (red) interacting with the Rieske (yellow) and cyt c_1 (blue) subunits. Cyt *b* (green) is in surface representation, and the other subunits are shown as ribbons with interacting side chains as sticks. The dashed boxes indicate the areas enlarged in panels (*C* and *D*). (*C*) Expanded view of the cytoplasmic side of SIV with residues mediating the interaction with the Rieske subunit labeled. (*D*) Expanded view of the lumenal side of SIV with residues mediating the interaction with cyt c_1 labeled.

with the Rieske TMH and the other with the cyt *b* subunit that interacts with the Rieske head domain. The other lipid is inserted in a pore between the Rieske TMH, cyt c_1, and cyt *b* subunits in the opposing monomer. The lipid head group is closely associated with the protein, and the tails extend toward the intermonomer cavity where they become disordered and can no longer be resolved (Fig. 4 *A*, *C*).

The remaining eight lipids were modeled on the cytoplasmic side of the complex, and their locations can be divided into three groups (Fig. 4*B*). There are two lipids bound within the central cavity of the complex that interact with both cyt *b* subunits (Fig. 4*D*). Two more lipids were resolved within a cavity between cyt *b* and the TMHs of SIV, the Rieske subunit and cyt c_1 monomer. One of these lipids interacts with the Rieske, cyt c_1, and SIV TMHs, and the second is bound to cyt *b* with one tail extending toward the Q_i site and the other toward the central cavity (Fig. 4*E*). On the opposite side of the complex, only the lipid interacting with cyt *b* was resolved (Fig. 4*B*). We note that density was apparent in the symmetrical location, but this was not of sufficient quality to allow confident assignment and was left unmodeled. Three additional lipids were modeled on the outside of the complex associated with the cyt *b* subunits on only one monomer; density features could not be assigned with any confidence on the other side of the complex (Fig. 4*F*).

Ubiquinone Bound to the Q_o Site and Conformational Changes in the Rieske Head Domain. Following modeling of the protein, cofactors, and lipids, an area of unassigned density that resembles a quinone headgroup with an isoprene tail was apparent (Fig. 5*A*). After fitting a ubiquinone-10 molecule and truncating the isoprene tail to fit the density, we found that the quinone/quinol was bound within the Q_o site. For a thorough interpretation of the structure, it is important to consider the quinone species bound to the Q_o site, which cannot be determined from density at the 2.9 Å resolution of the map. The samples were prepared predominantly in darkness to minimize quinol formation by the RCs. Following separation from the other complexes, the cyt bc_1 complexes had sufficient time to equilibrate to their resting state. Therefore, it is most likely that a quinone is bound at the Q_o site and His152 is protonated. This is consistent with previous work, where in the absence of inhibitors and excess quinone a gx = 1.800 signal is observed in electron paramagnetic resonance, which is assigned to the Q.ISPH from of the Q_o site (49). However, it is important to note that we cannot rule out unintended alterations of the redox state during cryo-EM grid preparation. The head group of the quinone is near the Rieske subunit, forming a hydrogen bond (3.2 Å) between the quinone methoxy oxygen and His152, which chelates the FeS cluster. As this oxygen has no exchangeable H, this is unlikely to be a redox active conformation. The redox active oxygen is 4.5 Å away from the His152 nitrogen, which is too far for proton transfer. Therefore, the quinone conformation is likely to represent a snapshot of quinone approach to, or egress from, the Q_o site rather than the enzyme-substrate complex. The position of the head group is close to that of the Q_o site inhibitor stigmatellin bound to the *R. sphaeroides* complex lacking SIV [PDB ID: 2QJP (38)] (*SI Appendix*, Fig. S4*A*). However, unlike for stigmatellin, Glu295 within the conserved PEWY motif is too distant to form a hydrogen bond (5.45 Å) because the sidechain has rotated away from the quinone head group (Fig. 5*A*, *Inset*). It has been suggested that while Glu295 is important for stigmatellin binding, movement of semiquinone during the catalytic cycle and proton release (50–54), it is not required to bind quinone, consistent with the Q_o quinone in our structure. The ubiquinone in our structure is bound slightly deeper within the Q_o site than in analogous structures of mitochondrial complex III with the Q_o site occupied [PDB ID:6Q9E (55), PDB ID:7RJA (56); *SI Appendix*, Fig. S4*B*], and in a similar position to menaquinone, in close proximity to the FeS cluster, in menaquinone-binding complexes (57). Therefore, the present structure may add a further snapshot of conformations representing the approach and binding of ubiquinol to the Q_o site within the cyt bc_1 complex. There is also a series of hydrophobic interactions along the length of the molecule in the cyt *b* subunit. These residues (cyt *b* Ile91, Met140, Ala141, Phe144, Met145, Gly158, Ile162, Val161, Trp179, Leu180, Leu197, Pro294, Phe298, Phe301 Tyr302, Leu305, Met336; opposing cyt *b* Ile63, Val64, Met67; Rieske Leu34, Ile35, Met38 and Cys151) line a hydrophobic channel that guides the quinol from within the membrane to the Q_o site at the membrane surface (Fig. 5 *A* and *B*). We note that other densities were present, both within the opposing Q_o site and within both Q_i sites, but they could not be reliably assigned and were left unmodeled.

The relatively low local resolution of the Rieske subunits may be indicative of dynamics in this subunit, so we performed focused classification to resolve distinct conformations. We began by creating a soft mask around the soluble domains of the Rieske subunits, then performing 3D classification without alignment. One of the three classes, comprising 72,118 particles, showed an alternative conformation for one Rieske head domain. Following unmasked refinement of this class without alignment, we were able to rigid-body dock the Rieske head domain in a new orientation, rebuild the loop that connects it to the TMH, locally sharpen the map using LocScale (47), and perform molecular dynamics flexible fitting with ISOLDE (58). The resulting map

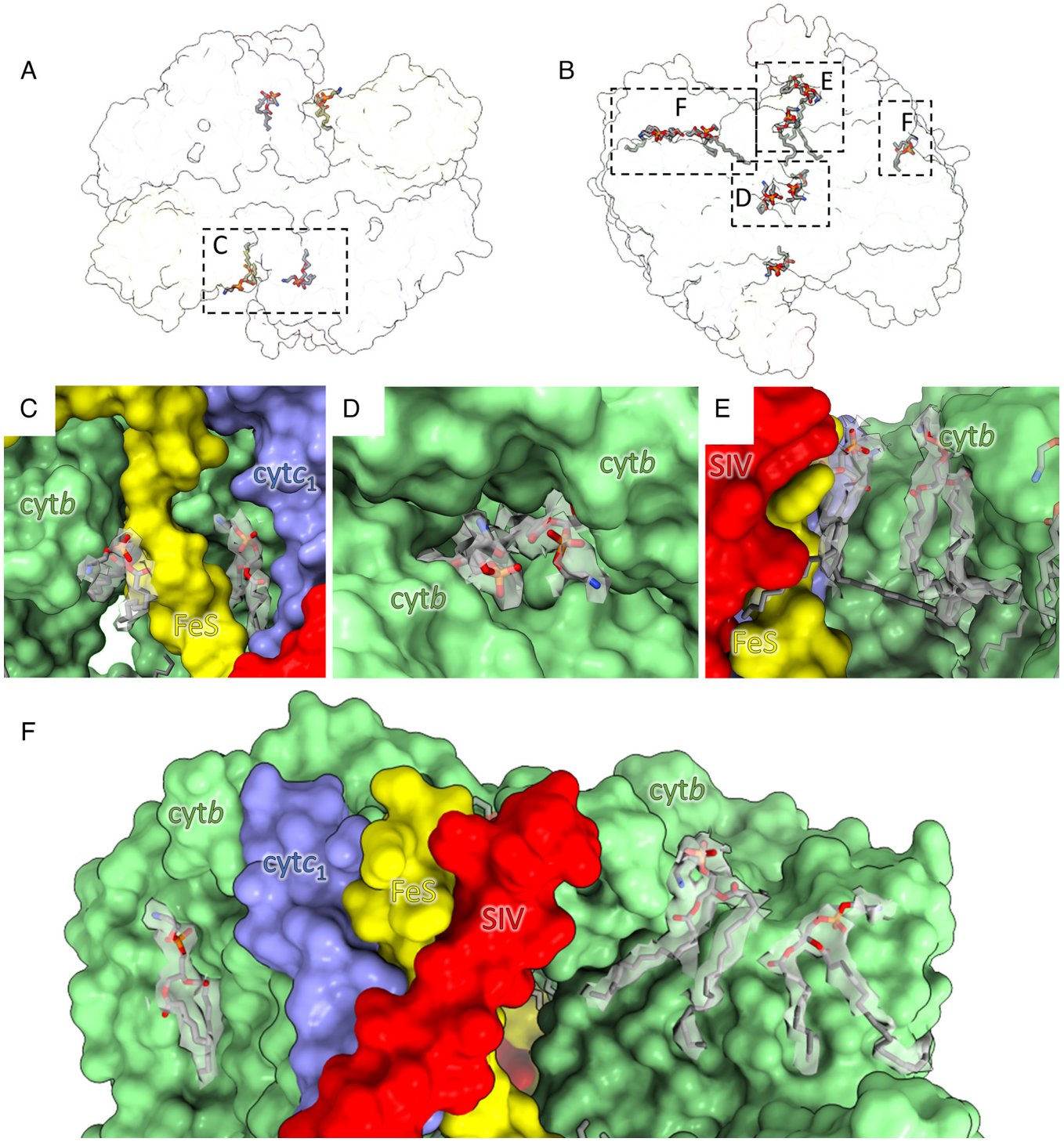

Fig. 4. Resolved lipids in the cyt bc_1 complex. (*A*) Cross-section of the complex displayed as a semi-transparent surface viewed from the lumenal side of the complex with lipids shown in stick representation. (*B*) Semi-transparent surface and lipids viewed from the cytoplasmic side of the complex. (*C*) Close-up view of one pair of lumenal lipids. The protein is shown in surface representation with each subunit labeled, and the lipids are shown in stick representation within their density, shown as a gray semi-transparent surface at threshold 0.012. (*D*) Expanded view of the cytoplasmic lipids at the center of the complex with density at threshold 0.007. (*E*) Expanded view of the cytoplasmic lipids in the central cavity at a threshold of 0.007. (*F*) Zoomed-in view of lipids on the cytoplasmic face of the complex with density at threshold 0.011. Color coding as in Fig. 2: SIV, red; cyt c_1, blue; Rieske ISP, yellow; cyt *b*, green.

(resolution at FSC 0.5 = 3.75 Å) is shown overlaid with the consensus map in Fig. 5 *C* and *D* and in Movie S1. One of the Rieske head domains has rotated, moving from a position where it is docked with the cyt *b* subunit (the *b*-position) to one where it points toward the cyt c_1 subunit (the *c*-position) (Fig. 5*D* and Movie S1). In contrast, both cyt *b* and cyt c_1 subunits, both SIVs, and the other Rieske subunit overlay almost exactly (Fig. 5 *C* and *D* and Movie S1). Comparison of the models reveals that the Rieske head domain has rotated 52° relative to the subunit in the *b*-position owing to a rearrangement of the flexible linker between the head domain and the TMH. The rotation angle is slightly more than that observed in the *R. capsulatus* complex determined by cryo-EM (59), and slightly less than in the crystal structures of the *R. sphaeroides* and chicken cyt bc_1 complexes (12, 52, 60). A rotation of 56° was observed in molecular dynamics simulations (61), indicating that we have captured an intermediate state with the Rieske subunit

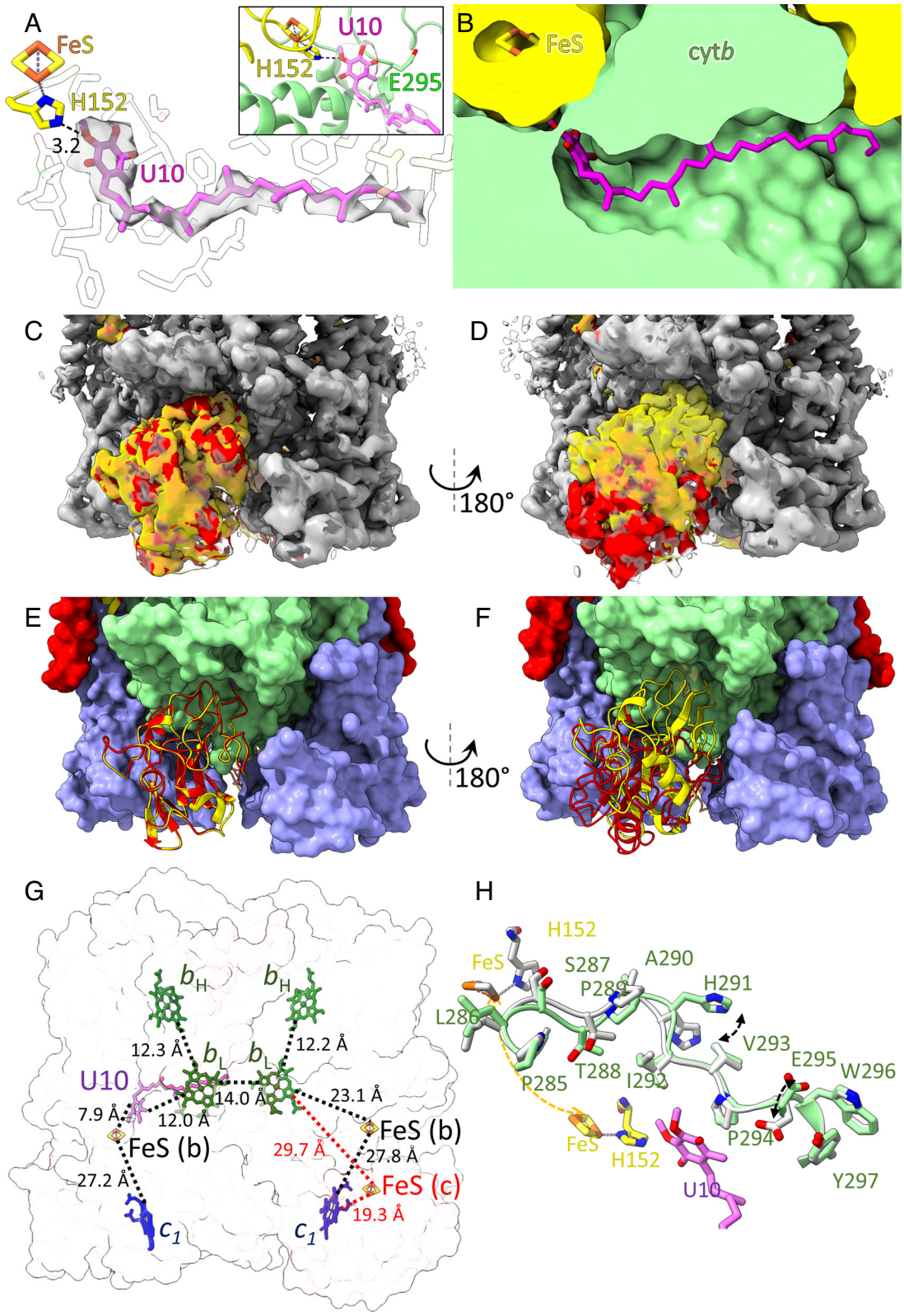

Fig. 5. Resolved quinone at the Q_o site and Rieske subunit dynamics. (*A*) Ubiquinone-10 (U10, magenta) within its density from the unsharpened map at threshold 0.07 (semi-transparent gray surface). The hydrogen bond to Rieske His152 is shown with a black dashed line and labeled with its distance. Other interacting residues are shown with semi-transparent sticks. The inset shows the proximity of U10 to Glu295, which is too distant for hydrogen bonding. (*B*) A cut-away surface view showing the ubiquinone binding pocket. (*C*) Overlaid locally sharpened consensus and focused-class maps. The static cyt *b* and cyt c_1 subunits and SIV are shown in gray, and the Rieske subunits are shown in semi-transparent yellow and solid red for the consensus map and the focused-class map, respectively. (*D*) The maps shown in panel *C* rotated 180° to show the mobile Rieske subunit. (*E*) Refined model of the focused-class with all subunits in surface representation except the near Rieske subunits, which are both resolved in the *b*-position, shown as cartoons. (*F*) The model in *E* rotated 180 degrees. The yellow Rieske subunit is resolved in the *b*-position, and the red subunit has rotated into *c*-position. (*G*) Hemes, FeS clusters, and U10 shown in stick representation. Closest edge-to-edge distances are shown in dashed black lines for the consensus structure, and red lines for the FeS cluster when the Rieske subunit is in the *c*-position. (*H*). Overlays of cyt *b* residues 285 to 297 in the apo (gray) and holo (color) Q_o sites from the focused and consensus classes, respectively. A movie showing morphs between the two structures in this figure is provided in the Movie S1.

almost fully shifted toward the *c*-position. The model also reveals that the stationary Rieske domain interacts with the bound Q_o quinone, while the mobile Rieske domain is on the side of the complex containing an unoccupied Q_o site (Fig. 5*C*–*G*). This suggests that the interactions between His152 and the bound quinone (Fig. 5*A*) bias the Rieske subunit toward the cyt *b* proximal conformation, whereas when the Q_o site is in the apo state, the Riseke subunit is free to adopt a wider range of conformations.

Fig. 5*G* and the Movie S1 show overlays of the cofactors and quinone in both structures with closest edge-to-edge distances labeled. All distances except those between the FeS cluster on the mobile side and its neighboring heme b_L and heme c_1 are identical. In the *b* position, the FeS cluster is 27.8 Å from heme c_1 and 23.1 Å from heme b_L. Following rotation into the *c* position the distance to heme c_1 decreases to 19.3 Å and the distance to heme b_L increases to 29.7 Å. On the opposing, static side of the complex, the quinone is located between the FeS cluster and heme b_L. The edge-to-edge distance to the FeS cluster is 7.9 Å and the distance to heme b_L is 12.0 Å. The remaining cofactors are found in the same arrangement observed in other cyt bc_1 structures and facilitate rapid electron transport via the low-potential chain toward the Q_i site (62), and intermonomer electron transfer via heme b_L (63, 64). Fig. 5*H* shows alignments of residues 185 to 297 of the cyt *b* subunit between the quinone-bound Q_o site in the consensus structure, and the unoccupied site in the focussed refined structure. There is a clear rearrangement of the cyt *b* lumenal loop (residues 285 to 296) with a notable shift in the position of His291 and of Glu295, which has rotated into the apo Q_o site.

Discussion

Interactions of Subunit IV with Other Components of the Cyt bc_1 Complex. The fourth subunit of the *R. sphaeroides* cyt bc_1 has long been known to be necessary for its optimal function, but the structure has remained elusive owing to its absence from crystal structures (38, 65). By combining purification of the complex in native nanodiscs with cryo-EM, we have resolved the structure of the TMH of SIV. The topology of SIV is in good agreement with previous studies, which demonstrated that the soluble N-terminal domain is located within the cytoplasm and the C-terminal region comprises a single TMH flanked by a small soluble lumenal domain (29, 31–33). In contrast to previous proposals that SIV interacts with the cyt *b* subunit, we show that its TMH lies across those of the Rieske and cyt c_1 subunits. Structural alignments with mitochondrial cyt bc_1 complexes reveal that SIV occupies a position similar to that adopted by the 7.2-kDa supernumerary subunit in the mitochondrial cyt bc_1 complex (yeast QCR9 or mammalian UQCR10) (PDB ID:1BGY (13), *SI Appendix*, Fig. S5), which is required for correct incorporation of the Rieske subunit and to stabilize the dimeric complex (66–69). Intriguingly, the acidic C-terminal region of yeast QCR9 is not needed for function, meaning its TMH appears be the major functional domain (66). This suggests that the TMH of SIV may serve to stabilize the complex, strengthening the interactions with the Rieske TMH and, consequently, the dimer interface. This is in keeping with reports that cyt bc_1 complexes from *R. sphaeroides* mutants lacking SIV are more labile following solubilization with dodecyl maltoside detergent (30). SIV and QCR9/UQCR10 do not share significant sequence similarity, suggesting they have evolved independently to fulfil their roles. We note that structural alignments of our four-subunit cyt bc_1 complex with the plant and cyanobacterial cyt b_6f complexes [PDB IDs 6RQF and 7R0W (70, 71)] reveal the absence of an equivalent of the *R. sphaeroides* SIV in cyt b_6f.

Usui and Yu previously indicated that the TMH of SIV interacted with quinones using radiolabeled quinone derivatives (29). Chen et al. showed that mutation of Trp79, which is the first residue we resolved on the cytoplasmic face of the membrane, impaired activity of the complex by ~75%, and raised the K_m for quinol fourfold (35). This residue is distant from the quinone/quinol binding sites and lies at the entrance to the intermonomer cavity, interacting with lipids that bridge to the Q_i site. In combination, these previous studies and the present structure indicate that Trp79 may be involved in transient interactions that guide quinones diffusing from the quinone pool to the Q_i binding pocket.

The primary structure of SIV has been the subject of intense previous characterization. Wu and Niederman performed partial digestion of the four-subunit cyt bc_1 and liberated a 9- to 10-kDa fragment of SIV, which corresponds to the 9.6-kDa mass of the unresolved region. Intriguingly they found that the ubiquinol-cyt *c* reductase activity of the complex was not diminished following digestion (31). Deletion of *fbc*Q from the genome results in cyt bc_1 complexes with activity decreased by 75% and a 4.3-fold increase in K_m for quinol (30). It was also shown that SIV was specifically produced during photosynthetic growth and that its deletion did not impede growth under aerobic conditions, suggesting SIV is specifically incorporated into cyt bc_1 complexes in chromatophores (30). Chen et al. later showed that activity could be restored with a plasmid-encoded copy of SIV and that residues 1 to 5 and 113 to 124 (a predicted small C-terminal soluble region), which were not resolved in our structure, were not required. Deletion of other residues in the soluble domain resulted in incorrect or no incorporation of SIV, suggesting that the N-terminal domain is required for the assembly and stability of SIV in vivo (37). In a later study, Chen et al. purified the three-subunit complex from a SIV-deficient strain and reconstituted it with SIV produced recombinantly in *Escherichia coli*, which restored almost all ubiquinol-cyt *c* reductase activity at a stoichiometric ratio. Tso et al. performed reconstitutions with truncated SIV peptides and showed that the transmembrane region was absolutely required for restoration of activity (36). Loss of the first 41 amino acids did not impede activity, while ~50% recovery was achieved with fragments containing the TMH between residues 77 to 109 (37). Further investigation by Tso et al. showed that the YRYR motif (residues 81 to 84) was essential, two residues of which (Tyr83 and Arg84) make protein–protein interactions in our structure (Fig. 3). Together, these studies indicate that interactions of the transmembrane region of SIV give rise to most of its function. The susceptibility of the N-terminal domain to proteases along with the finding that much of it is not required for normal activity suggests that it makes minimal, if any, interactions with the rest of the complex in mature cyt bc_1, explaining why it is flexible and unresolved in our maps. Additional functions cannot be discounted for the soluble domain, for example interacting with other proteins or complexes. One example could be the universal stress protein-1, which enhances cyt bc_1 activity and reduces superoxide production in the presence of SIV (72).

The Role of Subunit IV in Increasing the Rate of ATP Production of a Photosynthetic Vesicle. By combining our present structure with the results of previous studies, we can propose a function for SIV. By binding to the TMHs of the Rieske subunit and cyt c_1, SIV enhances the stability of the complex, and also increases its activity (29) (Fig. 1*E*) and lowers the production of damaging superoxide (34). Under aerobic growth, particularly under oxygen-limiting conditions, SIV is not required, either because the activity of the three-subunit cyt bc_1 is sufficient to

sustain respiratory electron transport, or because interactions with cyt *c* oxidase and cyt c_y to form supercomplexes provide their own set of stabilizing interactions (59, 73). However, under photosynthetic conditions, the RC can reduce quinol and oxidize cyt c_2 at a higher rate than during respiratory electron flow, even at relatively low light intensities (4, 5, 9). The assembly of a dimeric RC-LH1 core complex in *R. sphaeroides* (74–76) elevates the efficiency of energy trapping (77), placing more importance on the downstream oxidation of quinols generated by the RC. By incorporating the supernumerary SIV, which raises the maximum turnover rate of the cyt bc_1 complex up to threefold, and by positioning the cyt bc_1 complex in a lipid-rich domain adjacent to the RC (4, 5, 40, 46), *R. sphaeroides* has maximized this step in the overall conversion of absorbed light energy to ATP. However, the turnover of the enhanced four-subunit cyt bc_1 is still rate-limiting for the overall process of ATP synthesis when viewed from the perspective of the whole chromatophore vesicle (4, 5, 9). A photosynthetic chromatophore comprises on average 67 LH2 complexes, 11 RC–LH1 dimers, 2 RC–LH1 monomers, 4 cyt bc_1 dimers, and 2 ATP synthases (4). It has been suggested that the prevailing stoichiometry of approximately three RC-LH1 dimers to one cyt bc_1 dimer limits pmf generation by cyt bc_1 complexes, thereby offering protection against damage to the membrane vesicle by over-acidification. Another beneficial aspect of this stoichiometry is the overcapacity of ATP synthase activity, which is more than threefold higher than that required to consume the protons generated by the cyt bc_1 complexes (10). In summary, the activity of the four-subunit cyt bc_1 is optimized at the level of single complexes, but is also necessarily suboptimal at the level of a whole chromatophore vesicle. Thus, because cyt bc_1 activity is the kinetic bottleneck for converting light energy to ATP, the acquisition of SIV has raised ATP production by a photosynthetic vesicle almost threefold. The only other possibility of achieving a similar outcome for a vesicle would be to overcome the bottleneck by assembling threefold more cyt bc_1 complexes that lack SIV, which would be substantially more costly for the cell.

Binding of a Native Quinone within the Q_o Site of the Cyt bc_1 Complex. The RMSD of our consensus structure to the three-subunit complex with bound stigmatellin and antimycin (PDB ID:2QJP) was 0.460 Å, showing that transition to a detergent environment does not induce major conformational rearrangements within the complex. One notable difference is a small shift of the N-terminal region of the Rieske TMH, which is likely to accommodate the binding of SIV, and a small difference in the position of the Rieske hydrophilic domains (*SI Appendix*, Fig. S6). Because of the enhanced stability afforded by the native nanodisc assembly, and the ability to sample native conformational flexibility in cryo-EM datasets, we chose to exclude inhibitors from our preparations, and to process the data without imposing symmetry. This resulted in an asymmetric model where one of the Q_o sites had clear density for a bound quinone, while the other had weak density that could not be unambiguously assigned. A hydrogen bond between the Q_o quinone and His152 in the Rieske head domain locks it in the *b*-position with the FeS cluster close to the Q_o site. This interaction has previously been described in crystal structures with stigmatellin bound at Q_o (*SI Appendix*, Fig. S4) (12, 38, 52). Focused refinement revealed alternative conformations in the Rieske subunit proximal to the apo Q_o site, whereby rotation of the Rieske head domain to the *c*-position moves the FeS cluster closer to the *c*-heme within cyt c_1 (Fig. 5*G*). This conformation is similar to that observed by Steimle et al. for the *R. capsulatus* cyt bc_1 complex determined by cryo-EM (59), and cyt bc_1 complexes from various other species with a range of inhibitors bound (12, 60). A shift to the *c*-position after reduction of the FeS cluster following electron transfer from quinol significantly accelerates forward electron transfer to heme c_1 while preventing the unwanted back reaction in which an electron returns to the quinone in the Q_o site or to heme b_L, ensuring high efficiency of the bifurcated electron transfer that underpins the Q-cycle (52, 61, 78).

Structural alignments of the apo and holo Q_o sites revealed a conformational shift in the loop of the cyt *b* subunit spanning residues 285 to 297, that includes the PEWY motif. The most notable differences are the rotation of His291, which involves a small rearrangement of the backbone to accommodate the new conformation, and a rotation of Glu295 into the apo Q_o site. These changes are similar to those observed in crystal structures of the *R. sphaeroides* complex with either stigmatellin or azoxystrobin bound (60). A rotation of the PEWY glutamate was also observed in the chicken structure with either stigmatellin or myxothiozol bound (Glu272), but the rest of the loop is largely similar between the two structures (50, 52). Previous studies have shown that both Glu295 and His291 are necessary for proton release during oxidation of quinol at the Q_o site in bacterial complexes (50, 79). Therefore, the conformational differences we observe between the holo and apo sides of our structure may represent conformational changes involved in proton channelling during turnover. The observation of conformational rearrangements highlights the benefits of combining cryo-EM and native nanodiscs, and of not imposing symmetry on the maps for observing dynamics and quinone/quinol binding in these complexes. These approaches will be applicable to other cyt bc_1 and cyt b_6f complexes, and many other membrane-intrinsic protein complexes.

Concluding Remarks. In summary, the structure of the four-subunit cyt bc_1 complex of *R. sphaeroides* resolves many previously open questions surrounding the structure and function of SIV and reveals a correlation between quinone/quinol binding at the Q_o site and conformational changes in the Rieske head domain. Our structure provides intriguing insights into how and why supernumerary subunits of cyt bc_1 have evolved, and in particular how the acquisition of a single protein component of a rate-limiting complex can elevate the photosynthetic production of ATP.

Materials and Methods

Generation of Strains. Genomic modifications were made using the pK18mob*sacB* plasmid as previously described (80). The 3′ end of *znuC* (rsp_3568) was modified by addition of two premature stop codons seven residues before the C terminus. This was achieved by overlap extension PCR with primers to amplify the mutated end of the gene with ~400-bp upstream and downstream flanking genomic DNA (*SI Appendix*, Table S3). The sequence was ligated into pK18mob*sacB* using restriction enzymes EcoRI and HindIII, and the resulting plasmid was conjugated into *R. sphaeroides* harboring a His_{10}-tagged cyt c_1 (4) using *E. coli* S17-1. Correctly modified strains were isolated following sequential selection and counter selection steps with kanamycin (30 μg/mL) and sucrose (10% w/w), respectively, and were verified by PCR and automated Sanger sequencing (Eurofins).

The fbcQ (rsp_2687) gene was deleted from the strain containing the truncated ZnuC modification by amplifying ~400-bp regions upstream and downstream of *fbcQ* and joining them by overlap extension PCR, yielding a genomic sequence lacking the SIV coding region (*SI Appendix*, Table S3). The resulting PCR fragment was cloned into pK18mob*sacB* and used to delete the *fbcQ* gene as described above.

Preparation of cyt bc_1 in Native Nanodiscs. Purification of cyt bc_1 was performed by adapting our previous method (40) to enhance both purity and yield of the complex. *R. sphaeroides* cells were grown to stationary phase under photosynthetic conditions in 9 L M22 media (81) under ~50 μmol m^{-2} s^{-1} illumination from 70 W Phillips Halogen Classic bulbs. This corresponds to an optical density

at 650 nm of ~5 for the strains with SIV and ~3 for those lacking SIV due to their impaired photosynthetic growth. Cells were harvested by centrifugation at 4,000 RCF for 30 min at 4 °C then resuspended in 30 mL working buffer (20 mM Tris-HCl pH 8 containing 200 mM NaCl). Following addition of a few crystals of DNaseI and lysozyme, cells were broken via two passes through a cell disruptor (Constant Systems, UK) at 20,000 PSI followed by removal of unbroken cells and insoluble debris by centrifugation at 25,000 RCF for 15 min at 4 °C. To separate the membranes, the supernatant was centrifuged at 150,000 RCF for 2 h at 4 °C, and the soluble fraction was discarded. The pigmented membrane pellets were resuspended in 20 mL working buffer and homogenized. Cyt bc_1 was solubilized by diluting membranes to an absorbance at 850 nm of 50 in working buffer containing 1.5 % w/w SMA [prepared as described previously (82)] and incubating at room temperature for 1 h in the dark with gentle stirring. Insoluble material was removed by centrifugation at 150,000 RCF for 1 h at 4 °C, and the soluble fraction was diluted twofold prior to binding to a 50 mL Ni-NTA column preequilibrated in five column volumes (CVs) of working buffer by recycling for 16 h at a flow rate of 5 mL min^{-1}. The column was washed with ten CVs of working buffer containing 10 mM imidazole then cyt bc_1 was eluted over a linear gradient of 10 to 250 mM imidazole over six CVs collecting 5 mL fractions. UV/Vis/NIR spectra of pigmented fractions were collected between 350 and 1,000 nm, and those with a Soret band between 413 and 415 nm and a ratio of absorbance between 415 and 850 nm above 1 were concentrated to ~1 mL using a 100,000 MWCO Amicon centrifugal filter (Merck). Cyt bc_1 was further enriched by applying 0.5 mL to a 11 mL 10 to 15% w/w sucrose gradient in working buffer and centrifuging at 100,000 RCF for 16 h at 4 °C. The pigmented bands at ~12% sucrose were fractionated, spectra were collected between 250 and 1,000 nm, and those with a Soret band at 414 to 415 nm and a ratio of absorbance between 415 and 850 nm above ten were pooled and concentrated to 1 mL. Cyt bc_1 was injected onto a HiPrep™ 16/60 Sephacryl® S-300 HR size exclusion column (Cytiva) preequilibrated with two CVs of working buffer and eluted over 1.5 CVs at 0.5 mL/min collecting 2.5 mL fractions. Fractions with a Soret band at 415 nm and a ratio of absorbance at 415 nm to 280 nm of 1.15 to 1.25 were retained. The absorbance in the 800 to 900 nm range corresponding to RC-LH1 and LH2 was negligible in the final preparation and could be disregarded. The samples were concentrated to a *b*-heme concentration of 15 μM and used immediately for cryo-EM grid preparation, or frozen using liquid nitrogen in working buffer containing 20% v/v glycerol and stored at −80 °C until required.

UV/Vis/NIR Spectroscopy. Spectra were collected between 250 and 1,000 nm on a Cary 60 spectrophotometer. Spectra of pure cyt bc_1 were collected immediately following dilution in working buffer. Next a few grains of potassium ferricyanide were added followed by a few grains of sodium D-ascorbate and finally a few grains of sodium dithionite, collecting new spectra ~30 s after the addition of each reagent. The *c* heme concentrations were determined using the ascorbate reduced minus ferricyanide oxidized spectrum with an extinction coefficient of 20 mM^{-1} for the 551 nm to 542 nm absorbance difference (83). The *b*-heme concentration was determined using the dithionite reduced minus ascorbate reduced spectra with an extinction coefficient of 28 mM^{-1} for abs560–abs574 (84). For all assays, the cyt bc_1 concentration was taken as [*b*-heme]/2.

Activity Assays. Oxidized cyt c_2 was prepared by mixing equine cyt c_2 (Merck) with a few grains of potassium ferricyanide, followed by removal of ferricyanide on a PD-10 desalting column (Cytiva). Removal of oxidant was confirmed by UV/Vis spectroscopy, and the cyt c_2 concentration was determined by reducing a small amount with sodium D-ascorbate and using an extinction coefficient of 29.5 mM^{-1} at 550 nm. Decylubiquinol was prepared by reduction with sodium dithionite in 50% v/v ethanol and extracted by phase-separation with hexane as previously described for decylplastoquinone (71). Decylubiquinol was dissolved in a minimum volume of DMSO, and the concentration was determined using an extinction coefficient of 4 mM^{-1} at 290 nm in ethanol (85).

Activity assays were performed using an OLIS RSM1000 spectrophotometer equipped with a USA-SF stopped flow cell operating in rapid-scanning mode at 25 °C with a scan rate of 31 s^{-1} between 350 and 700 nm with 300 line mm^{-1}/500-nm blaze gratings, a 1.24-mm entrance slit, and 0.6-mm exit slit. Solution A contained 625 nM cyt bc_1 and 62.5 μM oxidized cyt c_2. Solution B contained 1.25 mM decylubiquinol. The solutions were mixed in a 4:1 ratio to give final concentrations of 500 nM cyt bc_1, 50 μM cyt c_2 and 250 μM decylubiquinol. Initial linear rates were determined using OLIS Global Works and Microsoft Excel software packages with a cyt c_2 red-ox extinction coefficient of 21 mM^{-1} at 550 nm.

Cryo-EM Grid Preparation. Quantifoil 1.2/1.3 300 mesh Cu grids (EM Resolutions Ltd.) were glow discharged at a current of 10 mA for 12 s under a partial atmosphere of air using a Cressington 208 glow discharge unit. A 5 μL volume of 15 μM cyt bc_1 was applied to the carbon-coated side of the grid and incubated at 18 °C with 80% relative humidity for 30 s, blotted for 4 s, and then plunge frozen in liquid ethane at −178 °C. Grids were screened using a Talos Arctica FEG TEM operating at an accelerating voltage of 200 kV equipped with Falcon III direct electron detector at 78,000 × magnification and a defocus of −3 μm. Grids with uniform thin ice and good particle density within the holes were selected for data collection.

Cryo-EM Data Collection. A total of 15,867 movies were collected on an FEI Titan Krios equipped with a Gatan K3 direct electron detector operating in super resolution mode with an energy filter slit width of 20 eV and an accelerating voltage of 300 kV. The nominal magnification was 130,000×, yielding an imaging resolution of 0.651 Å per physical pixel at the detector. Movies were collected over a 1.13 s exposure and fractionated into 40 frames with a dose of 1 e^{-} $Å^{-2}$ $frame^{-1}$ for a total dose of 40 e^{-} $Å^{-2}$. The applied defocus ranged between −0.8 and −2.0 μm in 0.3 μm steps.

Cryo-EM Data Processing. Data processing was performed using Relion 3.1 (86) unless otherwise stated. Movies were motion corrected using Relion's implementation of MotionCorr2 (87) with dose weighting using 5 × 5 patches and a B factor of 150, followed by CTF estimation using CTFFind 4.1.14 (88) within Relion. 4,060,135 particles were picked using crYOLO 1.7.5 (89) using a model trained with 10 motion corrected micrographs. Particles were extracted in 360-pixel boxes (downscaled to 120 pixels) and subjected to five rounds of reference-free 2D classification (T = 1.3, 540 classes in the final round), selecting those classes that have features corresponding to a nanodisc encapsulated complex of ~16 × 12 × 10 nm after each round. The final selected 2D classes contained 1,452,666 particles (35.8%). Next, a de novo initial model was generated using the stochastic gradient descent method with three classes, and the best class was used as a reference for 3D classification following removal of strong signal at the mask edge in UCSF ChimeraX 1.3 (90). The particles were subjected to two rounds of 3D classification (T = 4, 10 classes in round 2), yielding a single class with clear secondary structure features comprised of 282,636 particles (7.0%). Particles from this class were reextracted in 396-pixel boxes downscaled to 220 pixels (corresponding to a pixel size of 1.1718 Å at the specimen level) and subjected to multiple rounds of 3D refinement with two rounds of per-particle CTF refinement (fitting magnification, defocus, astigmatism, B-factor, phase-shift, beam tilt, trefoil and fourth order aberrations) and one round of per-particle motion correction. The final map after masking solvent (extending by 3 pixels and applying a 3-pixel soft edge) and postprocessing had a global resolution of 2.9 Å (FSC = 0.143). Selected 2D and 3D classes are shown in *SI Appendix*, Fig. S7, and FSC curves are shown in *SI Appendix*, Fig. S8.

Model Building and Refinement. An initial model was generated by downloading an existing *R. sphaeroides* cyt bc_1 structure from the PDB (PDB ID: 2QJP (38)) and removing inhibitors, waters, detergents, and ions. The model was docked into the map using the "Fit in map" tool in ChimeraX 1.3 (90) and manually refined in Coot v0.9.6 (91). The model was subtracted from the map to visualize unmodeled regions, which revealed two clear alpha-helical segments on each side of the complex. These were modeled by fitting a polyalanine helix into the map, then mutating the side chains to give best-fit to the density while considering the local environment using the SIV sequence as a reference, then manually building missing regions. Next, lipids and quinones were modeled into the remaining density and truncated to give a reasonable fit. The complete model was further optimized using the ISOLDE 1.2 plugin for ChimeraX (58) followed by final real-space refinement in Phenix v1.19.2 (92). Following local sharpening of the map in LocScale (47) the model was further refined using Coot, ISOLDE, and Phenix. Validation statistics are displayed in *SI Appendix*, Table S1.

Focused 3D Classification and Refinement. To analyze the refined particles for movements in the Rieske head domain, a soft mask was generated in ChimeraX 1.3. A surface was generated for residues 45 to 187, and a mask was generated on the grid of the postprocessed map extending by six pixels and padding by three

pixels using the "volume onesmask" command. The mask was used for 3D classification on the refined particles with the complete map as a reference with the following settings: T = 160, 3 classes, 25 iterations and image alignment disabled. The three classes contained 72,118 (24.6% of refined particles), 79,575 (27.2%), and 140,943 (48.2%) particles. Particles from class 1, which displayed a distinct conformation for one Rieske subunit, were selected and subjected to 3D refinement without alignment followed by masking and postprocessing. The other two classes were near identical to the consensus map and not processed further. The Rieske head domain from the consensus model was reoriented to give best fit to the new map, the linker to the TMH was rebuilt in Coot, and the model was subjected to the same refinement procedure using Coot, ISOLDE, and Phenix described for the consensus model. Because disabling alignment is problematic for gold standard FSC calculations, we quote the resolution at an FSC of 0.5 (*SI Appendix*, Fig. S9 for the FSC curves), which was 3.75 Å for class 1. Validation statistics are displayed in *SI Appendix*, Table S1.

Confirmation of Cyt bc_1 Subunit Composition by Mass Spectrometry. Proteins were extracted by precipitation from purified cyt bc_1 complex and digested with pepsin as previously described (93). The resultant peptide fragments were analyzed by nanoflow liquid chromatography–mass spectrometry (94) using a 75-min reverse-phase gradient for peptide separation. Protein identification was as previously described (93).

Data, Materials, and Software Availability. The structures and EM maps have been deposited in the protein data bank (PDB) and electron microscopy data bank (EMDB) with the following accession IDs: Consensus refinement with the Rieske domain in the *b*-position: PDB ID: 8ASI (95), EMDB: EMD-15616 (96). Focussed class with the Riseke domains in the *b*- and *c*- positions: PDB ID: 8ASJ (97), EMDB: EMD-15617 (98). The mass spectrometry proteomics data have been deposited to the ProteomeXchange Consortium via the PRIDE partner repository (http://proteomecentral.proteomexchange.org) with the dataset identifier PXD039340 (99). All study data are included in the article and/or *SI Appendix*.

ACKNOWLEDGMENTS. D.J.K.S, E.C.M, and C.N.H were supported by Biotechnology and Biological Sciences Research Council (BBSRC) UK, award number BB/M000265/1, and European Research Council Synergy Award 854126. D.J.K.S was also supported by the University of East Anglia new investigator start-up funding. F.R.H. was supported by a Diamond Light Source PhD studentship (number STU0355) jointly funded by the University of Sheffield. A.H. is supported by a Royal Society University Research Fellowship, which also funds a PhD studentship to J.H.S. (award number URF\R1\191548). D.A.F and C.A.S. acknowledge Diamond Light Source for access and support of the cryo-EM facilities at the UK's national Electron Bio-Imaging Centre at Diamond Light Source under proposal nr29785. M.P.J. acknowledges support from the BBSRC (award number BB/V006630/1) and the Leverhulme Trust (Grant RPG-2019-045).

Author affiliations: [a]School of Biological Sciences, University of East Anglia, Norwich NR4 7TJ, United Kingdom; [b]Plants, Photosynthesis and Soil, School of Biosciences, University of Sheffield, Sheffield S10 2TN, United Kingdom; and [c]Diamond Light Source Ltd, Didcot OX11 0DE, United Kingdom

1. A. R. Crofts, S. W. Meinhardt, K. R. Jones, M. Snozzi, The role of the quinone pool in the cyclic electron-transfer chain of *Rhodopseudomonas sphaeroides*: A modified Q-cycle mechanism. *Biochim. Biophys. Acta* **723**, 202–218 (1983).
2. P. Mitchell, Protonmotive redox mechanism of the cytochrome *b*-c_1 complex in the respiratory chain: Protonmotive ubiquinone cycle. *FEBS Lett.* **56**, 1–6 (1975).
3. T. Geyer, V. Helms, Reconstruction of a kinetic model of the chromatophore vesicles from *Rhodobacter sphaeroides*. *Biophys. J.* **91**, 927–937 (2006).
4. M. L. Cartron *et al.*, Integration of energy and electron transfer processes in the photosynthetic membrane of *Rhodobacter sphaeroides*. *Biochim. Biophys. Acta* **1837**, 1769–1780 (2014).
5. A. Singharoy *et al.*, Atoms to phenotypes: Molecular design principles of cellular energy metabolism. *Cell* **179**, 1098–1111.e23 (2019).
6. L. A. Malone, M. S. Proctor, A. Hitchcock, C. N. Hunter, M. P. Johnson, Cytochrome b_6f – Orchestrator of photosynthetic electron transfer. *Biochim. Biophys. Acta* **1862**, 148380 (2021).
7. A. N. Tikhonov, The cytochrome b_6f complex at the crossroad of photosynthetic electron transport pathways. *Plant Physiol. Biochem.* **81**, 163–183 (2014).
8. S. S. Hasan, W. A. Cramer, On rate limitations of electron transfer in the photosynthetic cytochrome b_6f complex. *Phys. Chem. Chem. Phys.* **14**, 13853–13860 (2012).
9. A. Hitchcock, C. N. Hunter, M. Sener, Determination of cell doubling times from the return-on-investment time of photosynthetic vesicles based on atomic detail structural models. *J. Phys. Chem. B* **121**, 3787–3797 (2017).
10. M. Sener, J. Strumpfer, A. Singharoy, C. N. Hunter, K. Schulten, Overall energy conversion efficiency of a photosynthetic vesicle. *Elife* **5**, e09541 (2016).
11. W. Yamori *et al.*, The roles of ATP synthase and the cytochrome b_6f complexes in limiting chloroplast electron transport and determining photosynthetic capacity. *Plant Physiol.* **155**, 956–962 (2011).
12. Z. Zhang *et al.*, Electron transfer by domain movement in cytochrome bc_1. *Nature* **392**, 677–684 (1998).
13. S. Iwata *et al.*, Complete structure of the 11-subunit bovine mitochondrial cytochrome bc_1 complex. *Science* **281**, 64–71 (1998).
14. P. O. Ljungdahl, J. D. Pennoyer, D. E. Robertson, B. L. Trumpower, Purification of highly active cytochrome bc_1 complexes from phylogenetically diverse species by a single chromatographic procedure. *Biochim. Biophys. Acta* **891**, 227–241 (1987).
15. G. Zhu *et al.*, A 3.3Å-resolution structure of hyperthermophilic respiratory complex III reveals the mechanism of its thermal stability. *Angew. Chem. Int. Ed. Engl.* **59**, 351–359 (2020).
16. D. Yang, Y. Oyaizu, H. Oyaizu, G. J. Olsen, C. R. Woese, Mitochondrial origins. *Proc. Natl. Acad. Sci. U.S.A.* **82**, 4443–4447 (1985).
17. R. C. Prince, P. L. Dutton, A kinetic completion of the cyclic photosynthetic electron pathway of *Rhodopseudomonas sphaeroides*: Cytochrome *b*-cytochrome c_2 oxidation-reduction. *Biochim. Biophys. Acta* **387**, 609–613 (1975).
18. D. P. O'Keefe, P. L. Dutton, Cytochrome *b* oxidation and reduction reactions in the ubiquinone-cytochrome b/c_2 oxidoreductase from *Rhodopseudomonas sphaeroides*. *Biochim. Biophys. Acta* **635**, 149–166 (1981).
19. S. W. Meinhardt, A. R. Crofts, Kinetic and thermodynamic resolution of cytochrome c_1 and cytochrome c_2 from *Rhodopseudomonas sphaeroides*. *FEBS Lett.* **149**, 223–227 (1982).
20. R. C. Prince, P. L. Dutton, Single and multiple turnover reactions in the ubiquinone-cytochrome *b*-c_2 oxidoreductase of *Rhodopseudomonas sphaeroides*. The physical chemistry of the major electron donor to cytochrome c_2, and its coupled reactions. *Biochim. Biophys. Acta* **462**, 731–747 (1977).
21. K. Takamiya, R. C. Prince, P. L. Dutton, The recognition of a special ubiquinone functionally central in the ubiquinone-cytochrome *b*-c_2 oxidoreductase. *J. Biol. Chem.* **254**, 11307–11311 (1979).
22. J. R. Bowyer, P. L. Dutton, R. C. Prince, A. R. Crofts, The role of the Rieske iron-sulfur center as the electron donor to ferricytochrome c_2 in *Rhodopseudomonas sphaeroides*. *Biochim. Biophys. Acta* **592**, 445–460 (1980).
23. P. L. Dutton, J. B. Jackson, Thermodynamic and kinetic characterization of electron-transfer components in situ in *Rhodopseudomonas spheroides* and *Rhodospirillum rubrum*. *Eur. J. Biochem.* **30**, 495–510 (1972).
24. A. R. Crofts, The modified Q-cycle: A look back at its development and forward to a functional model. *Biochim. Biophys. Acta* **1862**, 148417 (2021).
25. L. Yu, Q. C. Mei, C. A. Yu, Characterization of purified cytochrome *b*-c_1 complex from *Rhodopseudomonas sphaeroides* R-26. *J. Biol. Chem.* **259**, 5752–5760 (1984).
26. D. J. Purvis, R. Theiler, R. A. Niederman, Chromatographic and protein chemical analysis of the ubiquinol-cytochrome c_2 oxidoreductase isolated from *Rhodobacter sphaeroides*. *J. Biol. Chem.* **265**, 1208–1215 (1990).
27. L. Yu, C. A. Yu, Essentiality of the molecular weight 15,000 protein (subunit IV) in the cytochrome bc_1 complex of *Rhodobacter sphaeroides*. *Biochemistry* **30**, 4934–4939 (1991).
28. K. M. Andrews, A. R. Crofts, R. B. Gennis, Large-scale purification and characterization of a highly active four-subunit cytochrome bc_1 complex from *Rhodobacter sphaeroides*. *Biochemistry* **29**, 2645–2651 (1990).
29. S. Usui, L. Yu, Subunit IV (Mr = 14,384) of the cytochrome *b*-c_1 complex from *Rhodobacter sphaeroides*. Cloning, DNA sequencing, and ubiquinone binding domain. *J. Biol. Chem.* **266**, 15644–15649 (1991).
30. Y.-R. Chen, S. Usui, C.-A. Yu, L. Yu, Role of subunit IV in the cytochrome *b*-c_1 complex from *Rhodobacter sphaeroides*. *Biochemistry* **33**, 10207–10214 (1994).
31. J. Wu, R. A. Niederman, Topological organization of the Rieske iron-sulphur protein and subunit IV in the cytochrome bc_1 complex of *Rhodobacter sphaeroides*. *Biochem. J.* **305**, 823–828 (1995).
32. L. Yu, C. A. Yu, Identification of cytochrome *b* and a molecular weight 12K protein as the ubiquinone-binding proteins in the cytochrome *b*-c_1 complex of a photosynthetic bacterium *Rhodobacter sphaeroides* R-26. *Biochemistry* **26**, 3658–3664 (1987).
33. E. Wilson, T. M. Farley, J. Y. Takemoto, Photoaffinity labeling of an antimycin-binding site in *Rhodopseudomonas sphaeroides*. *J. Biol. Chem.* **260**, 10288–10292 (1985).
34. Y. Yin, S. C. Tso, C. A. Yu, L. Yu, Effect of subunit IV on superoxide generation by *Rhodobacter sphaeroides cytochrome* bc_1 complex. *Biochim. Biophys. Acta* **1787**, 913–919 (2009).
35. Y. R. Chen, S. K. Shenoy, C. A. Yu, L. Yu, Identification of amino acid residues involved in structural and ubiquinone-binding functions of subunit IV of the cytochrome bc_1 complex from *Rhodobacter sphaeroides*. *J. Biol. Chem.* **270**, 11496–11501 (1995).
36. S. C. Tso, Y. Yin, C. A. Yu, L. Yu, Identification of amino acid residues essential for reconstitutive activity of subunit IV of the cytochrome bc_1 complex from *Rhodobacter sphaeroides*. *Biochim. Biophys. Acta Bioenerg.* **1757**, 1561–1567 (2006).
37. S. C. Tso, S. K. Shenoy, B. N. Quinn, L. Yu, Subunit IV of cytochrome bc_1 complex from *Rhodobacter sphaeroides*. Localization of regions essential for interaction with the three-subunit core complex. *J. Biol. Chem.* **275**, 15287–15294 (2000).
38. L. Esser *et al.*, Inhibitor-complexed structures of the cytochrome bc_1 from the photosynthetic bacterium *Rhodobacter sphaeroides*. *J. Biol. Chem.* **283**, 2846–2857 (2008).
39. T. Su, L. Esser, D. Xia, C. A. Yu, L. Yu, Generation, characterization and crystallization of a cytochrome c_1-subunit IV fused cytochrome bc_1 complex from *Rhodobacter sphaeroides*. *Biochim. Biophys. Acta* **1817**, 298–305 (2012).
40. D. J. K. Swainsbury *et al.*, Probing the local lipid environment of the *Rhodobacter sphaeroides* cytochrome bc_1 and *Synechocystis* sp. PCC 6803 cytochrome b_6f complexes with styrene maleic acid. *Biochim. Biophys. Acta Bioenerg.* **1859**, 215–225 (2018).

41. J. M. Dörr *et al.*, Detergent-free isolation, characterization, and functional reconstitution of a tetrameric K+ channel: The power of native nanodiscs. *Proc. Natl. Acad. Sci. U.S.A.* **111**, 18607–12 (2014).
42. D. J. K. Swainsbury, S. Scheidelaar, R. Van Grondelle, J. A. Killian, M. R. Jones, Bacterial reaction centers purified with styrene maleic acid copolymer retain native membrane functional properties and display enhanced stability. *Angew. Chemie. Int. Ed.* **53**, 11803–11807 (2014).
43. M. Orwick-Rydmark *et al.*, Detergent-free incorporation of a seven-transmembrane receptor protein into nanosized bilayer lipodisq particles for functional and biophysical studies. *Nano Lett.* **12**, 4687–4692 (2012).
44. C. Sun *et al.*, Structure of the alternative complex III in a supercomplex with cytochrome oxidase. *Nature* **557**, 123–126 (2018).
45. P. Kumar, G. D. Cymes, C. Grosman, Structure and function at the lipid–protein interface of a pentameric ligand-gated ion channel. *Proc. Natl. Acad. Sci. U.S.A.* **118**, e2100164118 (2021).
46. C. Vasilev *et al.*, FRET measurement of cytochrome bc_1 and reaction centre complex proximity in live *Rhodobacter sphaeroides* cells. *Biochim. Biophys. Acta* **1863**, 148508 (2022).
47. A. J. Jakobi, M. Wilmanns, C. Sachse, Model-based local density sharpening of cryo-EM maps. *Elife* **6**, e27131 (2017).
48. J. Jumper *et al.*, Highly accurate protein structure prediction with AlphaFold. *Nature* **596**, 583–589 (2021).
49. H. Ding, D. E. Robertson, F. Daldal, P. L. Dutton, Cytochrome bc_1 complex [2Fe-2S] cluster and its interaction with ubiquinone and ubihydroquinone at the Q_o site: a double-occupancy Q_o site model. *Biochemistry* **31**, 3144–3158 (1992).
50. A. R. Crofts *et al.*, Pathways for proton release during ubihydroquinone oxidation by the bc_1 complex. *Proc. Natl. Acad. Sci. U.S.A.* **96**, 10021–10026 (1999).
51. A. Osyczka *et al.*, Role of the PEWY glutamate in hydroquinone—quinone oxidation—reduction catalysis in the Q_o site of cytochrome bc_1. *Biochemistry* **45**, 10492–10503 (2006).
52. A. R. Crofts *et al.*, Mechanism of ubiquinol oxidation by the bc_1 complex: Different domains of the quinol binding pocket and their role in the mechanism and binding of inhibitors. *Biochemistry* **38**, 15807–15826 (1999).
53. D. Victoria, R. Burton, A. R. Crofts, Role of the -PEWY-glutamate in catalysis at the Q_o-site of the Cyt bc_1 complex. *Biochim. Biophys. Acta* **1827**, 365–386 (2013).
54. D.-W. Lee *et al.*, Zinc inhibition of bacterial cytochrome bc_1 reveals the role of cytochrome *b* E295 in proton release at the Q_o site. *Biochemistry* **50**, 4263–4272 (2011).
55. J. A. Letts, K. Fiedorczuk, G. Degliesposti, M. Skehel, L. A. Sazanov, Structures of respiratory supercomplex I+III_2 Reveal functional and conformational crosstalk. *Mol. Cell* **75**, 1131–1146.e6 (2019).
56. J. M. Di Trani *et al.*, Rieske head domain dynamics and indazole-derivative inhibition of *Candida albicans* complex III. *Structure* **30**, 129–138.e4 (2022).
57. W. C. Kao, C. Hunte, Quinone binding sites of cyt *bc* complexes analysed by X-ray crystallography and cryogenic electron microscopy. *Biochem. Soc. Trans.* **50**, 877–893 (2022).
58. T. I. Croll, *ISOLDE*: A physically realistic environment for model building into low-resolution electron-density maps. *Acta Crystallogr. D Struct. Biol.* **74**, 519–530 (2018).
59. S. Steimle *et al.*, Cryo-EM structures of engineered active bc 1-cbb 3 type $CIII_2CIV$ super-complexes and electronic communication between the complexes. *Nat. Commun.* **12**, 929 (2021).
60. L. Esser, F. Zhou, C. A. Yu, D. Xia, Crystal structure of bacterial cytochrome bc_1 in complex with azoxystrobin reveals a conformational switch of the Rieske iron–sulfur protein subunit. *J. Biol. Chem.* **294**, 12007–12019 (2019).
61. S. Izrailev, A. R. Crofts, E. A. Berry, K. Schulten, Steered molecular dynamics simulation of the Rieske subunit motion in the cytochrome bc_1 complex. *Biophys. J.* **77**, 1753–1768 (1999).
62. A. R. Crofts, Z. Wang, How rapid are the internal reactions of the ubiquinol: Cytochrome c_2 oxidoreductase? *Photosynth. Res.* **22**, 69–87 (1989).
63. M. Świerczek *et al.*, An electronic bus bar lies in the core of cytochrome bc_1. *Science* **329**, 451–454 (2010).
64. R. Ekiert, M. Czapla, M. Sarewicz, A. Osyczka, Hybrid fusions show that inter-monomer electron transfer robustly supports cytochrome bc_1 function in vivo. *Biochem. Biophys. Res. Commun.* **451**, 270–275 (2014).
65. M. Elberry *et al.*, Generation, characterization and crystallization of a highly active and stable cytochrome bc_1 complex mutant from *Rhodobacter sphaeroides*. *Biochim. Biophys. Acta* **1757**, 835–840 (2006).
66. J. D. Phillips, L. A. Graham, B. L. Trumpower, Subunit 9 of the *Saccharomyces cerevisiae* cytochrome bc_1 complex is required for insertion of EPR-detectable iron-sulfur cluster into the Rieske iron-sulfur protein. *J. Biol. Chem.* **268**, 11727–11736 (1993).
67. V. Zara, I. Palmisano, L. Conte, B. L. Trumpower, Further insights into the assembly of the yeast cytochrome bc_1 complex based on analysis of single and double deletion mutants lacking supernumerary subunits and cytochrome *b*. *Eur. J. Biochem.* **271**, 1209–1218 (2004).
68. V. Zara, L. Conte, B. L. Trumpower, Identification and characterization of cytochrome bc_1 subcomplexes in mitochondria from yeast with single and double deletions of genes encoding cytochrome bc_1 subunits. *FEBS J.* **274**, 4526–4539 (2007).
69. I. Vercellino, L. A. Sazanov, Structure and assembly of the mammalian mitochondrial supercomplex $CIII_2CIV$. *Nature* **598**, 364–367 (2021).
70. M. S. Proctor *et al.*, Cryo-EM structures of the *Synechocystis* sp. PCC 6803 cytochrome b_6f complex with and without the regulatory PetP subunit. *Biochem. J.* **479**, 1487–1503 (2022).
71. L. A. Malone *et al.*, Cryo-EM structure of the spinach cytochrome b_6f complex at 3.6 Å resolution. *Nature* **575**, 535–539 (2019).
72. T. Su, Q. Wang, L. Yu, C. A. Yu, Universal stress protein regulates electron transfer and superoxide generation activities of the cytochrome bc_1 complex from *Rhodobacter sphaeroides*. *Biochemistry* **54**, 7313–7319 (2015).
73. O. Fedotovskaya *et al.*, Identification of a cytochrome bc_1-aa_3 supercomplex in *Rhodobacter sphaeroides*. *Biochim. Biophys. Acta* **1862**, 1–13 (2021).
74. P. Qian *et al.*, Cryo-EM structure of the dimeric *Rhodobacter sphaeroides* RC-LH1 core complex at 2.9 Å: The structural basis for dimerisation. *Biochem. J.* **478**, 3923–3937 (2021).
75. P. Cao *et al.*, Structural basis for the assembly and quinone transport mechanisms of the dimeric photosynthetic RC–LH1 supercomplex. *Nat. Commun.* **13**, 1977 (2022).
76. K. Tani *et al.*, Asymmetric structure of the native *Rhodobacter sphaeroides* dimeric LH1–RC complex. *Nat. Commun.* **13**, 1904 (2022).
77. M. Chenchiliyan *et al.*, Dimerization of core complexes as an efficient strategy for energy trapping in *Rhodobacter sphaeroides*. *Biochim. Biophys. Acta* **1857**, 634–642 (2016).
78. A. R. Crofts *et al.*, Mechanism of ubiquinol oxidation by the bc_1 complex: Role of the iron sulfur protein and its mobility. *Biochemistry* **38**, 15791–15806 (1999).
79. F. Francia *et al.*, The cytochrome *b* Zn binding amino acid residue histidine 291 is essential for ubihydroquinone oxidation at the Q_o site of bacterial cytochrome bc_1. *Biochim. Biophys. Acta* **1857**, 1796–1806 (2016).
80. G. A. Sutherland, P. Qian, C. N. Hunter, D. J. K. Swainsbury, A. Hitchcock "Engineering purple bacterial carotenoid biosynthesis to study the roles of carotenoids in light-harvesting complexes" in *Methods in Enzymology* (Academic Press, 2022). https://doi.org/10.1016/bs.mie.2022.04.001.
81. C. N. Hunter, G. Turner, Transfer of genes coding for apoproteins of reaction centre and light-harvesting LH1 complexes to *Rhodobacter sphaeroides*. *J. Gen. Microbiol.* **134**, 1471–1480 (1988).
82. D. J. K. Swainsbury *et al.*, The effectiveness of styrene–maleic acid (SMA) copolymers for solubilisation of integral membrane proteins from SMA-accessible and SMA-resistant membranes. *Biochim. Biophys. Acta* **1859**, 2133–2143 (2017).
83. P. M. Wood, The interrelation of the two *c*-type cytochromes in *Rhodopseudomonas sphaeroides photosynthesis*. *Biochem. J.* **192**, 761–764 (1980).
84. J. A. Berden, E. C. Slater, The reaction of antimycin with a cytochrome b preparation active in reconstitution of the respiratory chain. *Biochim. Biophys. Acta* **216**, 237–249 (1970).
85. Y. Hatefi, "COENZYME Q (UBIQUINONE)" in *Advances in Enzymology and Related Subjects of Biochemistry* (1963), pp. 275–328.
86. J. Zivanov *et al.*, New tools for automated high-resolution cryo-EM structure determination in RELION-3. *Elife* **7**, e42166 (2018).
87. S. Q. Zheng *et al.*, MotionCor2: Anisotropic correction of beam-induced motion for improved cryo-electron microscopy. *Nat. Methods* **14**, 331–332 (2017).
88. A. Rohou, N. Grigorieff, CTFFIND4: Fast and accurate defocus estimation from electron micrographs. *J. Struct. Biol.* **192**, 216–221 (2015).
89. T. Wagner *et al.*, SPHIRE-crYOLO is a fast and accurate fully automated particle picker for cryo-EM. *Commun. Biol.* **2**, 218 (2019).
90. E. F. Pettersen *et al.*, UCSF ChimeraX: Structure visualization for researchers, educators, and developers. *Protein Sci.* **30**, 70–82 (2021).
91. P. Emsley, B. Lohkamp, W. G. Scott, K. Cowtan, Features and development of *Coot*. *Acta Crystallogr. D Biol. Crystallogr.* **66**, 486–501 (2010).
92. P. D. Adams *et al.*, *PHENIX*: A comprehensive Python-based system for macromolecular structure solution. *Acta Crystallogr. Sect. D* **66**, 213–221 (2010).
93. P. Qian *et al.*, Cryo-EM structure of the monomeric *Rhodobacter sphaeroides* RC–LH1 core complex at 2.5 Å. *Biochem. J.* **478**, 3775–3790 (2021).
94. S. E. Flannery *et al.*, Developmental acclimation of the thylakoid proteome to light intensity in Arabidopsis. *Plant J.* **105**, 223–244 (2021).
95. D. J. K. Swainsbury *et al.*, Four subunit cytochrome *b*-c_1 complex from Rhodobacter sphaeroides in native nanodiscs - consensus refinement in the b-b conformation. Protein Data Bank. https://www.ebi.ac.uk/pdbe/entry/pdb/8ASI. Deposited 19 August 2022.
96. D. J. K. Swainsbury *et al.*, Four subunit cytochrome *b*-c_1 complex from Rhodobacter sphaeroides in native nanodiscs - consensus refinement in the b-b conformation. Electron Microscopy Data Bank. https://www.ebi.ac.uk/emdb/EMD-15616. Deposited 19 August 2022.
97. D. J. K. Swainsbury *et al.*, Four subunit cytochrome *b*-c_1 complex from Rhodobacter sphaeroides in native nanodiscs - focussed refinement in the b-c conformation. Protein Data Bank. https://www.ebi.ac.uk/pdbe/entry/pdb/8ASJ. Deposited 19 August 2022.
98. D. J. K. Swainsbury *et al.*, Four subunit cytochrome *b*-c_1 complex from Rhodobacter sphaeroides in native nanodiscs - focused refinement in the b-c conformation. *Electron Microscopy* Data Bank. https://www.ebi.ac.uk/emdb/EMD-15617. Deposited 19 August 2022.
99. D. J. K. Swainsbury *et al.*, Confirmation of the subunit composition of Rhodobacter sphaeroides cytochrome *b*-c_1 complex isolated in styrene maleic acid nanodiscs. ProteomeXchange Project. http://proteomecentral.proteomexchange.org/cgi/GetDataset?ID=PXD039340. Deposited 19 August 2022.